Journal of Structural Geology 173 (2023) 104908

Contents lists available at ScienceDirect

Journal of Structural Geology

journal homepage: www.elsevier.com/locate/jsg

Differential deformation of a strike-slip fault in the Paleozoic carbonate reservoirs of the Tarim Basin, China

Yingtao Yao [a,b], Lianbo Zeng [a,b,*], Zhe Mao [a,b], Jun Han [c], Dongsheng Cao [a,b], Bo Lin [c]

[a] State Key Laboratory of Petroleum Resource and Prospecting, China University of Petroleum (Beijing), Beijing, 102249, China
[b] College of Geoscience, China University of Petroleum (Beijing), Beijing, 102249, China
[c] Sinopec Northwest Oilfield Company, Urumqi, Xinjiang, 830011, China

ARTICLE INFO

Keywords:
Strike-slip fault
Geometric characteristics
Faulting time
Scaling law
Tarim basin

ABSTRACT

Ultra-deep carbonate reservoirs buried over 7000 m are distributed around strike-slip faults, which control hydrocarbon accumulation and enrichment in the Tarim Basin, China. This study proposes a fracture development index (FDI) method for analyzing the width of the strike-slip fault zone based on 3D seismic data. Based on the FDI method and geological and geophysical data, we analyze the structural characteristics of the SB5 strike-slip fault and the scaling of fault zone width and throw.

In map view, at depth the strike-slip fault is characterized by single fault segments, extensional overlaps, and contractional overlaps, at intermediate depths by left-stepping en echelon normal faults, and in shallow layers by right-stepping en echelon normal faults. In cross section, we find composite flower structures and positive flower structures and medium-shallow layer negative flower structures or deep layer negative flower structures and medium-shallow layer negative flower structures. The formation time of deep, middle, and shallow layer faults is the middle Caledonian, Late Caledonian, and Late Hercynian. The heterogeneity of the strike-slip fault zone varies from strong to weak from contractional overlaps, to extensional overlaps, and single fault segments. Strike-slip fault-related fractures are dominated by three sets intersecting with strike-slip faults at small angles. Where throw is less than 100 m, the fault zone width and throw have a good power law relationship. Where the throw is over 100 m, the width tends to diminish with throw.

1. Introduction

Strike-slip faults accommodating horizontal displacements in response to plate movements are common structures in the Earth's crust (e.g., Sylvester, 1988), reflecting the complex setting and history of horizontal slip (Storti et al., 2006; Brogi, 2011). Similar to other types of faults, strike-slip faults usually have complex structures and are formed by local shear in brittle rock formations, which are typically composed of narrow and highly deformed fault cores and wider damage zones (Chester et al., 1993; Kim et al., 2004; Agosta et al., 2012; Laubach et al., 2014). The fault core usually comprises fault rocks and develops structures such as fault gouge, fault breccia, and shear zones to accommodate displacement (Caine et al., 1996; Berg and Skar, 2005). The damage zone is a deformation zone rich in secondary faults and fractures related to interaction and connections between faults (Petit and Barquins, 1988; Choi et al., 2016). The geometric and kinematic characteristics of strike-slip faults can help us understand the formation of fault-controlled fractured reservoirs (Swanson, 2005; Share et al., 2019). The relationship between fault attributes, e.g., fault zone width and displacement, is essential for understanding the mechanical and physical processes of faulting (Evans, 1990; Scholz et al., 1993; Savage and Brodsky, 2011; Kolyukhin and Torabi, 2012; Roberts and Holdsworth, 2022). Furthermore, the timing and evolution of faults not only affect fluid flow but also have important implications for fault growth processes and nucleation (Sibson, 1989; Aydin, 2000; Delle Piane et al., 2017; Balsamo et al., 2019).

Oil and gas exploration and development have shown that the strike-slip faults in ultra-deep carbonate rocks play an important role in controlling the formation of reservoirs and the migration of oil and gas in the Tarim Basin, China (Yang et al., 2022). Ultra-deep carbonate reservoirs buried more than 7000 m are distributed around strike-slip faults, which are critical factors in hydrocarbon accumulation and reservoir development in deeply buried Ordovician carbonate reservoirs (Teng et al., 2020; Qi, 2021). Polyphase tectonic movements lead to

* Corresponding author. State Key Laboratory of Petroleum Resource and Prospecting, China University of Petroleum (Beijing), Beijing, 102249, China.
E-mail address: lbzeng@sina.com (L. Zeng).

https://doi.org/10.1016/j.jsg.2023.104908
Received 31 October 2022; Received in revised form 12 June 2023; Accepted 13 June 2023
Available online 14 June 2023

destruction of primary reservoir space in ultra-deep tight carbonate reservoirs, where the matrix (host rock) has no effective reservoir space. Reservoir space consists primarily of secondary structures such as fractures and dissolved pores along faults (Lyu et al., 2021). The physical properties of reservoirs in different locations of the strike-slip fault vary greatly, characterized by overall oil-bearing and uneven enrichment along the strike-slip faults (Qi, 2021).

Some studies have been conducted on geometric and kinematic characteristics of strike-slip faults in China. It is believed that strike-slip faults are mainly developed from the Cambrian to Permian strata, with segmentation in the map views and positive or negative flower structures in cross section (Han et al., 2017; Deng et al., 2019; Wang et al., 2020; Teng et al., 2020; Shen et al., 2022). The timing of strike-slip faults remains controversial. Some scholars believe that faults formed in the Ordovician (Wang et al., 2020; Shen et al., 2022), whereas others believe that faults formed in the Cambrian (Teng et al., 2020; Sun et al., 2021). In addition, the scaling of fault attributes has not been analyzed in the study area.

The SB5 strike-slip fault is the longest strike-slip fault in the Tarim Basin, extending from the Tazhong uplift to the Tabei uplift (Fig. 2). The geometric and kinematic characteristics of the southern and northern sections differ (Deng et al., 2019). The southern section has left-lateral motion, and the northern section has right-lateral motion. Several NE-striking left-lateral strike-slip faults intersect with the SB5 strike-slip fault (Fig. 2). The study of the SB5 strike-slip fault can provide a reference for the strike-slip faults of different tectonic belts in the Tarim Basin and inspection of these faults also helps to understand the tectonic evolution of the whole Tarim Basin. However, due to data limitations, our study analyzed the strike-slip fault characteristics of the northern section (Fig. 2).

Using the SB5 fault as an example, we propose a fracture development index (FDI) method for analyzing the widths of strike-slip fault zones based on 3D seismic data. We analyze the geometric and kinematic characteristics of strike-slip faults with depth using patterns evident in different structural layers. Based on cross-cutting relationships and geometric data, we document the timing of the fault and the heterogeneity of structural development. Finally, we discuss the relationship between the large-scale fault zone width and throw, and show how these abruptly vary with fault size.

2. Geological setting

The Tarim Basin, with an area of approximately 560,000 km^2, is one of China's most significant and earliest-developed petroliferous basins (Li et al., 1996). Southwest of the basin is the western Kunlun Mountains, north is the Tianshan Mountains, and southeast is the Altyn Tagh Mountains. Based on basement structure and sedimentary distribution, the Tarim Basin is divided into thirteen tectonic units (Fig. 1).

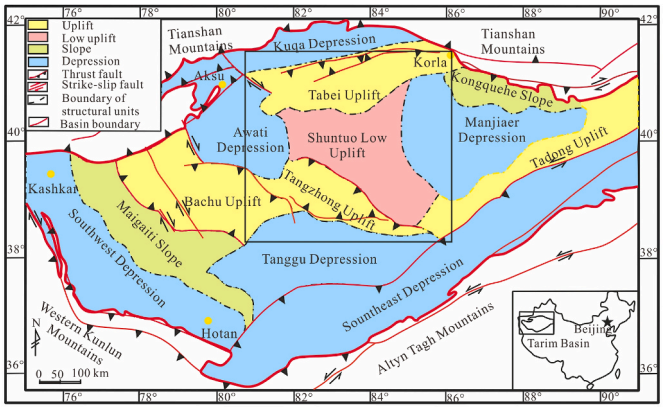

Fig. 1. The tectonic units in the Tarim Basin (modified from Li et al., 2013). The box represents the range of Fig. 2.

The Tarim block is a double-layer structure comprising a Precambrian basement and Neoproterozoic to Cambrian cap rock. It has experienced polyphase tectonic movements since its emergence. From the Cambrian to the Early Ordovician, the Tarim Craton transitioned from a stable sedimentary state to an extensional state due to the breakup of the Rodinia continent (Zhang et al., 2013; S.Z. Li et al., 2018). This extensional setting continued into the Middle Ordovician (Sobel and Arnaud, 1999). After the Late Ordovician, the collision between the western Kunlun and southwest Tarim blocks resulted in a series of NE-striking strike-slip faults (Yuan et al., 2002). After the Early Silurian, the Tarim Basin entered the post-collisional intraplate extension stage, and the pre-existing transpressional strike-slip faults were reactive (Wu et al., 2018; Zheng et al., 2019). From Late Devonian to Early Permian, the tectonic evolution of the Tarim Basin was mainly controlled by the subduction and shear closure of the South Tianshan Ocean from east to west, resulting in the reactivity of strike-slip faults (Klemd et al., 2011). Since the Jurassic, the Tarim Basin has been in a weak intra-continental extensional tectonic setting (Yu et al., 2014). The Tarim Basin has been affected mainly by the far-field stress of the collision between the Eurasian and Indian plates since the Neogene (Windley et al., 1990; Deng et al., 2019).

The stratigraphy of the Shuntuoguole area is relatively complete, including the Paleozoic, Mesozoic, and Cenozoic (Fig. 3). The main exploration and development targets are carbonate rocks of the Middle-Late Ordovician Yingshan Formation and Yijianfang Formation, which mainly develop granular limestone, micrite, and dolomite (Li et al., 2019). The primary reservoir space of the Yingshan and Yijianfang formations has been destroyed. The matrix porosity is mostly less than 2%, and the permeability is less than 1 mD, and the reservoir space is mainly secondary, comprising cavities, fractures, and dissolved pores along the strike-slip faults (Li et al., 2019; Lyu et al., 2021).

3. Data and methods

The nomenclature of surfaces in the Tarim basin is standardized (Fig. 3). Our study uses surfaces T_9^0 to T_5^0 to represent different stratigraphic layers (Fig. 3). Surfaces T_9^0, T_8^1, T_7^4, T_7^2, T_7^0, T_6^3, T_6^0, T_6^6, and T_5^0 are the top surface of the Sinian Qigebulake Formation, the top surface of the Late Cambrian Awatage Formation, the top surface of the Middle

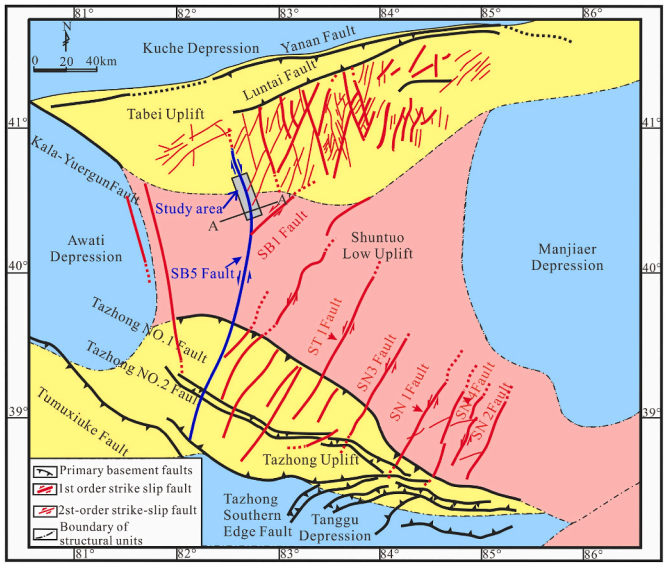

Fig. 2. The intracratonic strike-slip and basement faults on the top of the Middle Ordovician in the central and northern Tarim Basin. See Fig. 1 for the location. The grey box is the study area, representing the range of Fig. 8. Cross section A-A′ represents the cross section in Fig. 12.

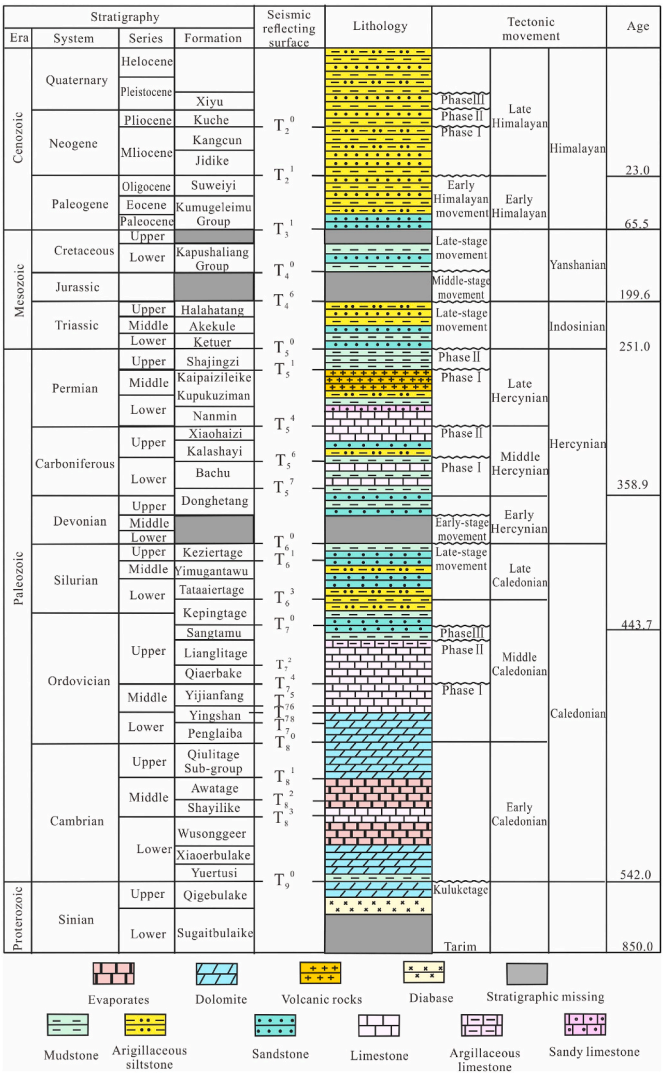

Fig. 3. Chart showing the stratigraphy, the seismic reflecting surfaces, and the timing of regional tectonic movements in the Tarim Basin (modified from Deng et al., 2019).

Ordovician Yijianfang Formation, the top surface of the Late Ordovician Qiaerbake Formation, the top surface of the Late Ordovician Sangtamu Formation, the top surface of the Late Silurian Kepingtage Formation, the top surface of the Late Silurian Keziertage Formation, the top surface of the Early Carboniferous Bachu Formation, and the top surface of the Late Permin Shajingzi Formation, respectively.

This study uses high-quality 3D seismic data to analyze the characteristics of the strike-slip fault. The main frequency of 3D seismic data is approximately 28 Hz. Geological and geophysical data were used to track surfaces. Several drilling and logging data in oil exploration and development synthesize seismograms for the well-seismic combinations. The seismic sections and key surfaces of coherence slices are used to analyze the characteristics of the strike-slip fault in cross sections and map views.

The fault throw and vertical separation are used to analyze geometry and kinematics (Fig. 4). The growth index is the ratio of unit thickness in the hanging wall and footwall strata (Childs et al., 2020). The statistics of the growth index of the normal faults enabled us to identify thickness variation between the hanging wall and footwall and limit the timing of the normal faults.

It is difficult to measure the horizontal displacement of strike-slip faults due to the limitations of seismic resolution. Many studies have indicated a good correlation between the width and displacement of the strike-slip faults (Mitchell & Faulkner, 2009; Faulkner et al., 2011; Savage & Brodsky, 2011). Therefore, based on 3D seismic data, we propose an analysis method of fracture development index (FDI) for analyzing the width of the strike-slip fault zone. The expression using the FDI to reflect the fault zone width is:

$$FDI = 1 - \frac{\lambda_{max}}{\sum_{j=1}^{J} \lambda_j} \quad (1)$$

Where FDI is the fracture development index, λ_{max} is the largest eigenvalue representing the dominant energy, and λ_j (j = 1, 2, …, J) is the jth eigenvalue of the covariance matrix. The greater the FDI, the higher the fracture intensity. Thus, FDI higher than the wall rock areas can be used to characterize the fault zone width (Fig. 5). The specific process is as follows: first, extracted the coherence attribute; then, a series of parallel and equidistant seismic survey lines perpendicular to the fault strike are selected, and each seismic survey line is resampled at an interval of 25 m. The FDI on each seismic survey line is calculated, and the variation law of the FDI is analyzed to determine the boundary between the fault damage zone and the wall rock areas.

Although by using the discontinuity generated by the fault zone the coherence attribute significantly improves the ability to identify faults, it is difficult to determine the exact location of the fault zone boundary because of the limitation of seismic resolution. Therefore, fracture density obtained from samples (thin sections), core observations, and image logs is compared with the FDI method to verify the reliability of the estimate.

The frequency of the damaged structure in the damage zone decreases with the distance from the fault core, and its boundary is usually shown as the location where the frequency of the fracture or deformation zone decreases to the background level (Berg and Skar, 2005; Mitchell & Faulkner, 2009; Choi et al., 2016). However, due to the influence of the subjective definition and the complexity of the damage zone structure (Choi et al., 2016), the boundary of each field measurement is different. To reduce the data uncertainty related to the width of

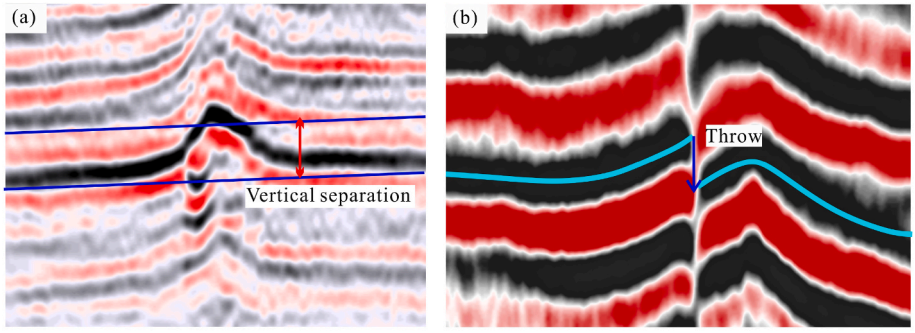

Fig. 4. Illustrated seismic section showing the fault attributes. (a) The seismic section shows the vertical separation. (b) The seismic section shows the throw.

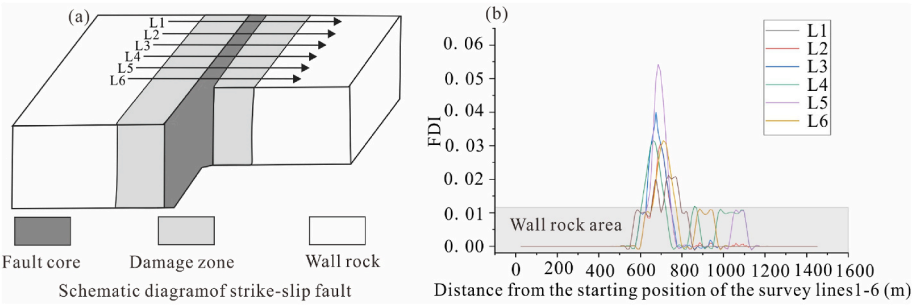

Fig. 5. Schematic diagram of analyzing the fault zone width using the fracture development index (FDI) method. (a) Schematic diagram of the strike-slip fault. Survey lines arrangement perpendicular to the fault strike. (b) Variations of FDI on different survey lines. L1 to L6 are the survey line numbers in Fig. 5a.

the fault zone, our study uses the cumulative fracture frequency method to define the boundary between the fault zone and the wall rock (Berg and Skar, 2005) and uses the cumulative frequency curve and its slope gradient to analyze the different degrees of deformation of the fault zone.

4. Results

4.1. Reliability of fracture development index (FDI) method

We analyzed the width of the fault zone using the FDI method. Taking well 1 as an example (Fig. 6), the cumulative fracture density shows changes in the slope gradient at 575 m and 750 m (Fig. 6b). We argue that the points at 575 m and 750 m should be the boundary of the fault damage zone. The outside of 575 m and 750 m have a similar gradient, representing the background value of the fault zone in the study area (Choi et al., 2016). The width of the fault zone is 175 m using the FDI method (Fig. 6b).

We analyzed the fracture density obtained by imaging logging and core data. The boundary of the fault zone is analyzed by using the fracture density variation along the well trajectory of the highly deviated well passing through the fault zone (Fig. 6c). The cumulative fracture density shows changes in the slope gradient at 7509.60 m, 7582.70 m, and 7730.50 m (Fig. 6d). We argue that point B at 7509.60 m and point C at 7730.50 m should be the boundary of the fault damage zone. The slope gradient at 7582.70 m increases within the fault zone, which may be related to the differential strain distribution inside the damage zone and is the transition zone between the damage zone and the wall rock (Micarelli et al., 2003; Choi et al., 2016). The highly deviated well is not horizontal. To accurately identify the fault zone boundary, we project points B and C in the direction perpendicular to the fault zone and get a width of 178.72 m.

The width of the fault zone is 175 m obtained by the cumulative FDI method (Fig. 6b). It is 3.72 m different from the results obtained by imaging logging and core data, with a slight difference between them. The main reasons for this difference are: (1) limitation of the seismic resolution leads to a certain uncertainty in accuracy; (2) limitation of survey line sampling interval because the interval used in this study is 25 m, which will lead to certain errors in the measurement results, but it can improve the processing efficiency. If the sampling interval is too small, it will lead to a large amount of data, which ordinary computers cannot calculate. Although there is a certain error between the FDI

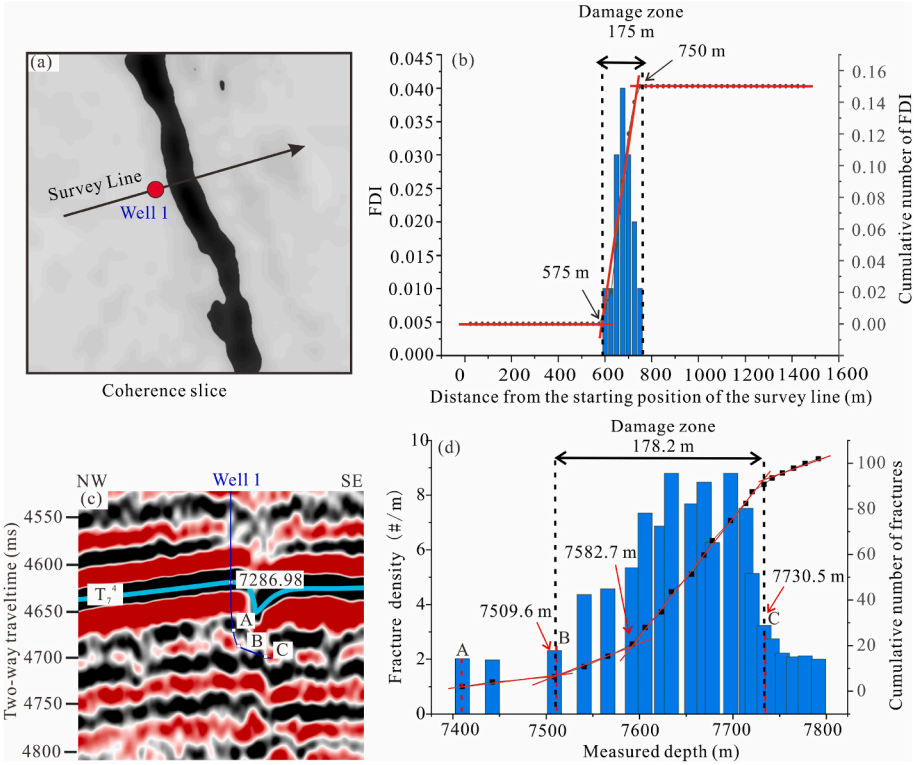

Fig. 6. The comparison between the fault zone width obtained by the FDI method based on 3D seismic data and the fault zone width obtained by well data. (a) Seismic survey lines through well 1 and perpendicular to the fault strike based on coherence slice on surface T_7^4. (b) Distribution of FDI based on cumulative methods of the survey line in Fig. 6a. (c) Seismic section through the well. (d) Fracture density distribution based on cumulative methods from points A to C. The position of points A to C corresponds to points A to C in Fig. 6c.

method and the fault zone width obtained by imaging and core data, the error is less than 5%, within an acceptable range. This method is believed to identify the width of the fault zone effectively.

4.2. Geometric and kinematic characterizations of the fault

The strike-slip faults have different structural characteristics in the deep layer, middle layer, and shallow structural layer. The deep layer structure develops from surfaces T_9^0 to T_7^0. The middle layer structure is between surfaces T_7^4 and T_6^0, and the shallow layer structure is between T_6^3 and T_5^0 (Fig. 7).

4.2.1. Deep layer structure

The deep layer structure has three distinct structural styles. The first is the single fault segment, which passes through the surface T_9^0 and T_7^4 from the bottom up, but not through surface T_7^0, and there is no vertical displacement on both sides of the fault (Fig. 7b and f). The second is the extensional stepover, which is developed between the right-stepping fault segments (Fig. 8B), and shown as a negative flower structure in the cross section (Fig. 7a and d), a negative flower structure consists of a shallow synform bounded by upward spreading strands of a wrench fault with mostly normal separations (Harding, 1985). The third is the contractional stepover (Fig. 8B), which is developed between the

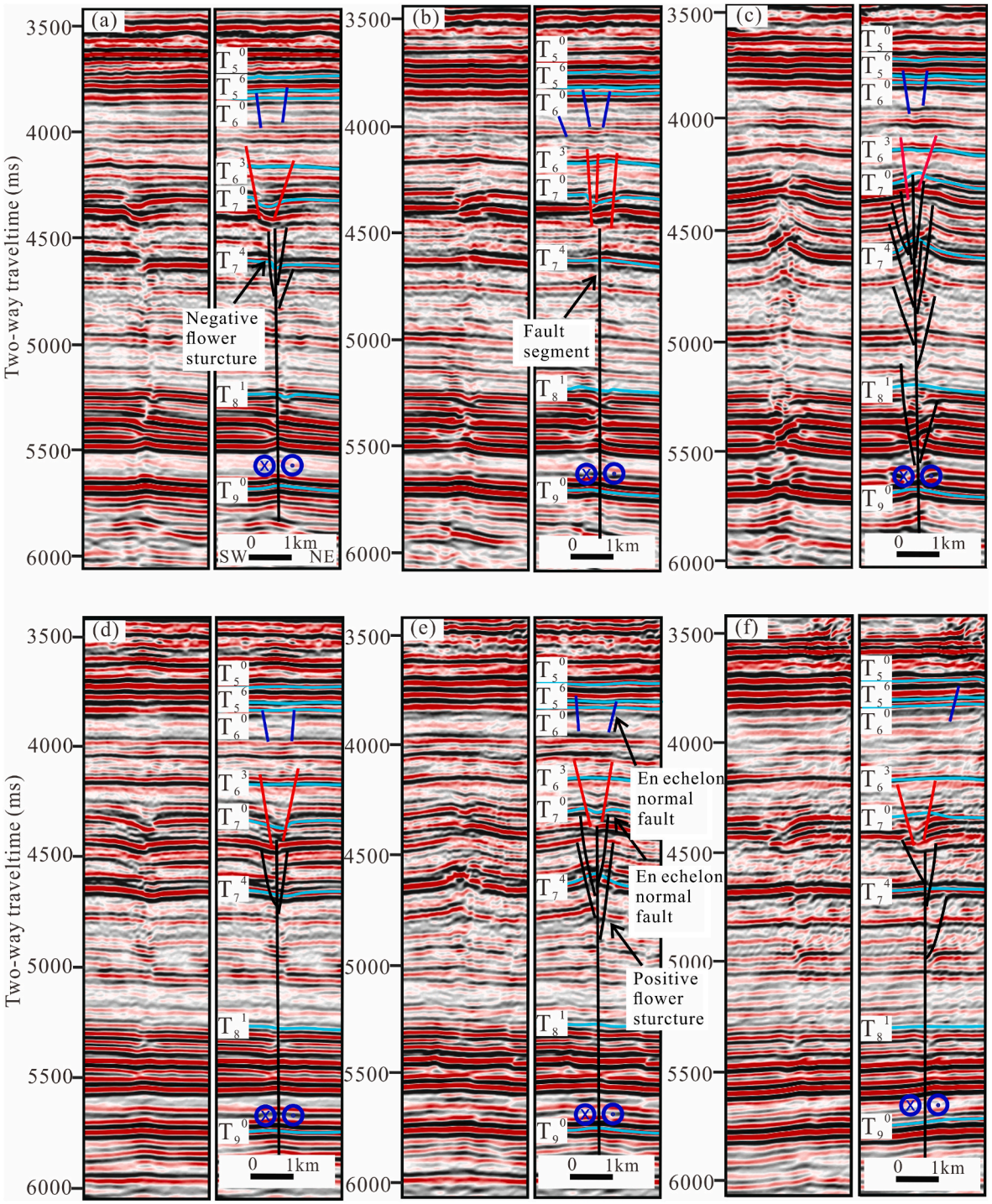

Fig. 7. Uninterpreted cross sections (left) and interpreted faults (right). The position of sections a to f is shown in the survey lines a to f in Fig. 8A.

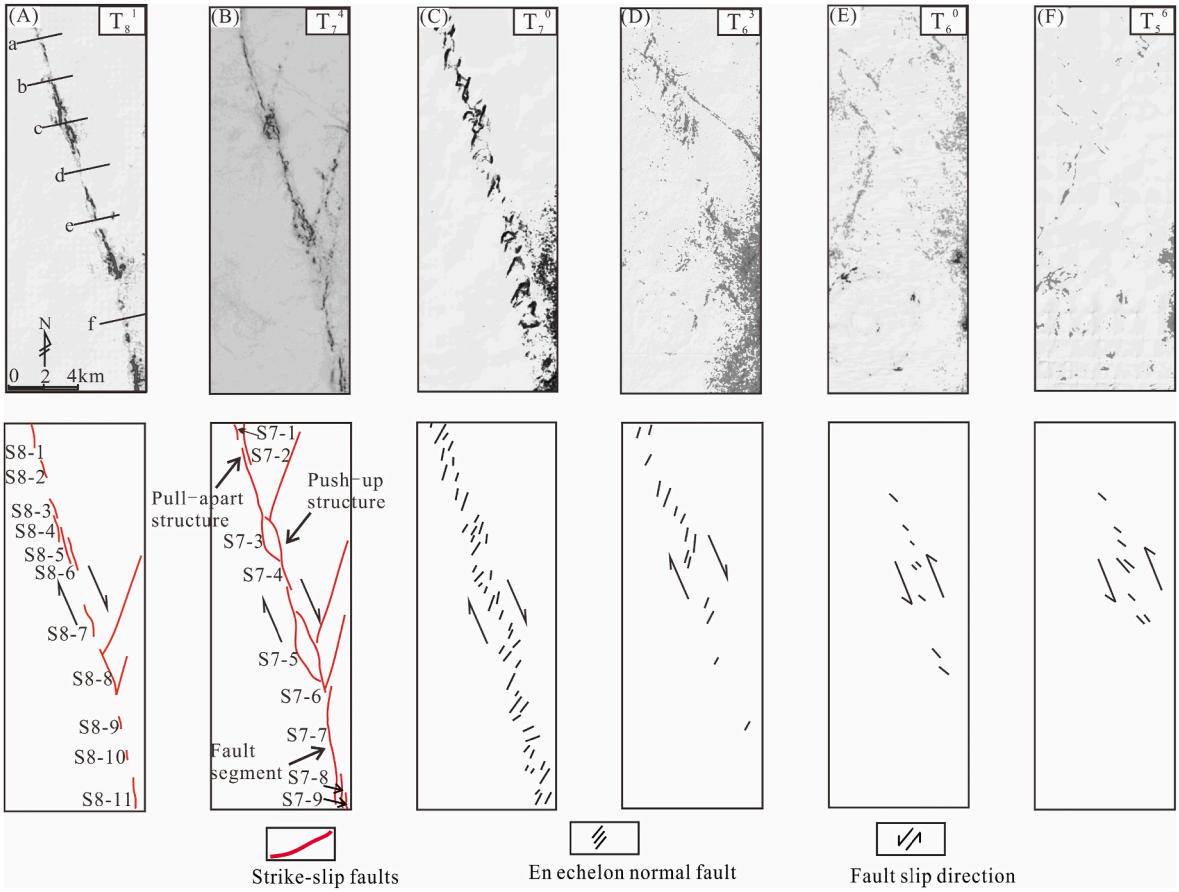

Fig. 8. Uninterpreted coherence slices (above) and interpreted faults (below) of the different surfaces. See Fig. 3 for the surfaces and the grey box in Fig. 2 for the locations. Survey lines a to f in Fig. 8A represent the locations of sections a to f in Fig. 7.

left-stepping fault segments and shows as a positive flower structure (Fig. 7c and f). A positive flower structure consists of a shallow antiform displaced by upward diverging strands of a wrench fault with mostly reverse separations (Harding, 1985). On surface T_7^4, the push-up structures between the left-stepping segments and pull-apart structures between the right-stepping segments (Fig. 8B) indicate right-lateral motion (Biddle & Christie-Blick, 1985).

This study counted the width and throw of the fault zone at the surface T_7^4 (Fig. 9). From survey line 1 to line 42, it can be found that the minimum width of the fault zone is 175 m, and the maximum is 1250 m, with an average is 539.97 m (Fig. 9b). The minimum throw is 23.04 m, and the maximum is 159.60 m, with an average is 74.42 m (Fig. 9b).

Local strata uplifts can be observed from surfaces T_9^0 to T_7^2, and the uplift disappeared after surface T_7^2 (Fig. 10b). Therefore, this study analyzed the vertical separation of different surfaces of the deep layer strike-slip fault. This study defines the extensional deformations as negative and the contractional deformations as positive. The results show that the vertical separation of surfaces T_9^0, T_8^1, T_7^4, and T_7^2 is 9 ms, 13 ms, 66 ms, and 53 ms, respectively; however, the vertical separation near surface T_7^0 becomes −32 ms (Fig. 10c).

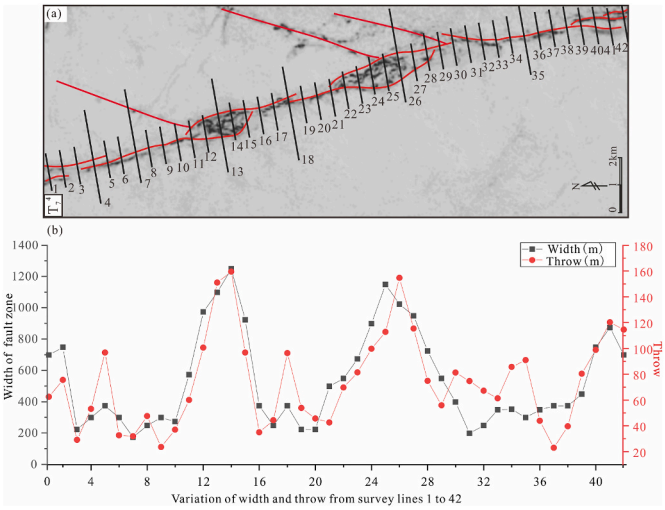

Fig. 9. Distribution of fault throws and widths along the fault strike. (a) Arrangement of lines 1 to 42 on surface T_7^4. Lines 1 to 42 indicate the number of seismic survey lines. (b) Variation of width and throw from survey lines 1 to 42 on surface T_7^4.

4.2.2. *Middle layer structure*

The middle layer structure is characterized by left-stepping en echelon normal faults in the map views (Fig. 8C and D) and negative flower structures in cross sections (Fig. 7). In cross sections, the normal faults are rarely connected with the deep layer structure, mostly in pairs (Fig. 7). It is worth noting that the normal faults partially overlap with the deep layer strike-slip fault, and the dip angle is between 70° and 90°. In the map view, the en echelon normal faults are distributed above the deep layer strike-slip fault segments; the strike of en echelon normal faults is mainly between N5E and N40E. Closer to surface T_7^0, more en echelon normal faults are shown (Fig. 8C). The distribution of en echelon normal faults has a significant difference in the north and south, en echelon normal faults are mainly distributed in the north (Fig. 8D). The left-stepping en echelon normal faults (Fig. 8C and D) indicate the right-

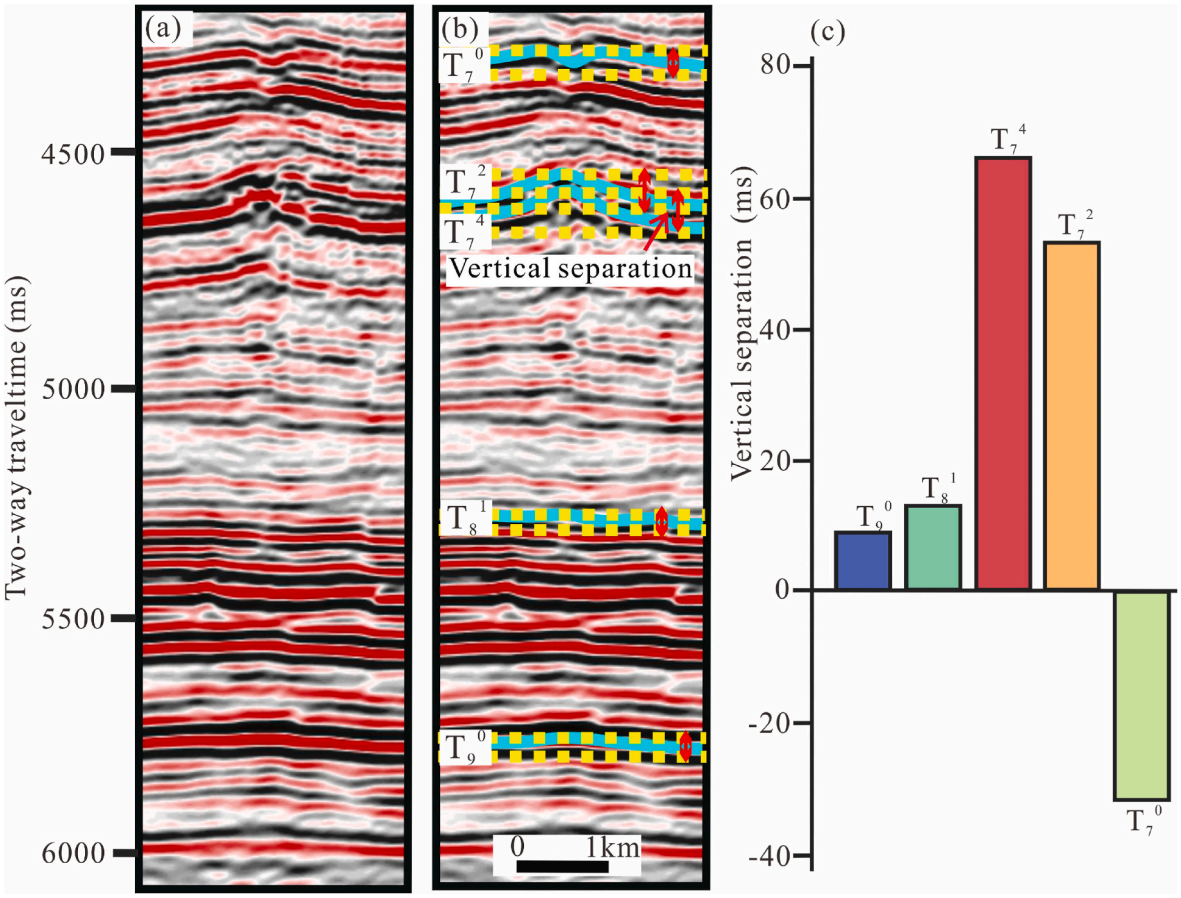

Fig. 10. Histogram showing the vertical separation of surfaces T_9^0 to T_7^0. (a) Uninterpreted cross section c. The position of the section is shown in the survey line c in Fig. 8A. (b) Interpreted vertical separation in Fig. 10a. (c) The vertical separation of different surfaces. Defining the extensional deformations as negative and the contractional deformations as positive.

lateral motion.

To better understand the kinematic characteristics of echelon normal faults, we calculated the fault growth index between surfaces T_7^4 and T_6^0. The growth index was calculated for the six sections in Fig. 5. There is a similar thickness below surface T_7^0, and the growth index is approximately 1.00. Between surfaces T_7^0 and T_6^3, the maximum growth index is 1.17, and the minimum is 1.05. The growth index of the en echelon normal faults between surfaces T_6^3 and T_6^0 ranged from 1.05 to 1.00 (Fig. 11).

4.2.3. Shallow layer structure

The shallow layer structure is characterized by the right-stepping normal faults with the strike of N45W to N30W in the map views (Fig. 8E and F), showing local negative flower structures in the cross sections (Fig. 7). The fault dip angle is between 60° and 90°, rarely connected to the middle layer normal faults; the normal faults pass through surfaces T_6^0 and T_5^6 upwards (Fig. 7), and locally crossed the Early-Middle Permian magmatic rocks (Liu et al., 2020; Ukar et al., 2020) (Fig. 12). The right-stepping normal faults indicate the left-lateral motion.

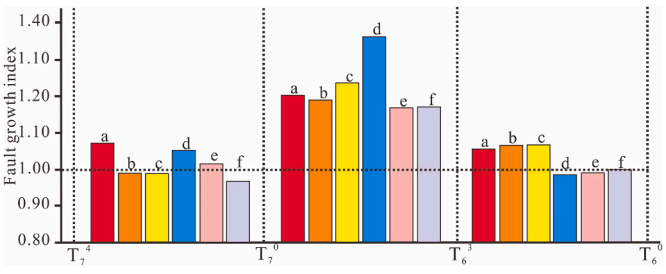

Fig. 11. The fault growth index from surfaces T_7^4 to T_6^0 in cross sections a-f. The position of sections a to f is shown in the survey lines a to f in Fig. 8A. Red to purple represent the growth index of cross sections a-f in Figs.7a to f, respectively. (For interpretation of the references to colour in this figure legend, the reader is referred to the Web version of this article.)

5. Discussion

5.1. Timing of the fault

The commonly used method for determining the timing of a fault is to analyze the cross-cutting relationship between the fault and strata; the timing of the fault is later than that of the cut strata and earlier than the strata that are not cut. We analyzed fault formation time using the cross-cutting relationships combined with the geometric characteristics of the fault.

5.1.1. Timing of deep layer structure

In the deep layer, the strike-slip faults pass upward through the surface T_7^4 but do not pass through surface T_7^0, indicating that the fault formed after the deposition of the Middle Ordovician Yijianfang Formation and before deposition of the Early Silurian Kepingtage Formation (Fig. 7).

The vertical separation from surfaces T_9^0 and T_7^2 is positive; however, the vertical separation near surface T_7^0 becomes negative (Fig. 10c). Suppose the strike-slip fault was formed before or during the Late Ordovician Lianglitage Formation. In that case, the sediment above the

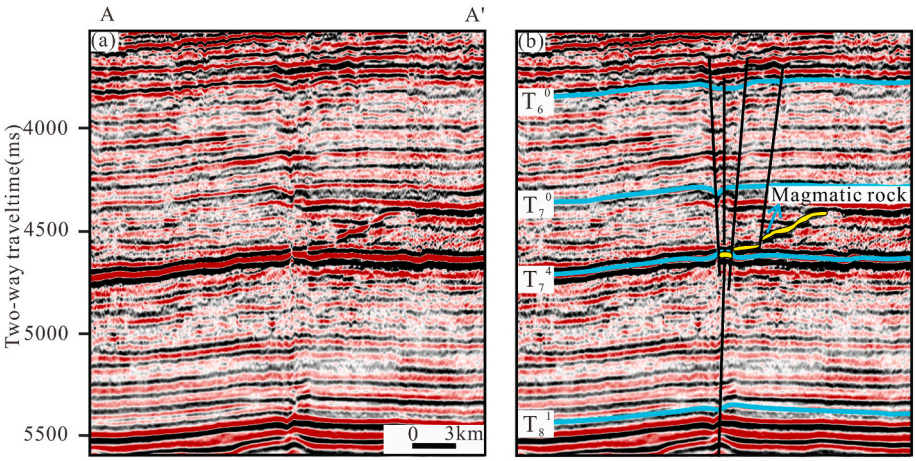

Fig. 12. Uninterpreted cross section a-a' (left) and interpreted cross-cutting relationship between faults and magmatic rocks (right). See cross section A-A′ in Fig. 2 for the location.

fault should have been deposited horizontally, resulting in an angular unconformity between the deformation layer and the later sediment. Because no such angular unconformity is observed in the cross sections (Fig. 10b), the deformation should have occurred after the sedimentation of the Late Ordovician Sangtamu Formation. Combined with the analysis of the cross-cutting relationships between faults and strata, we speculate that the strike-slip faults formed during the Late Ordovician.

Previous studies argued that the strike-slip faults formed in the Late Ordovician based on structural and geochemical analysis (Baqués et al., 2020; Ukar et al., 2020), which is consistent with the results of our study. The calcite cement fill within pull-apart void space is closely related to the timing of faults. The age of calcite cement fill within pull-apart void space can reflect the timing of fault movement (Roberts and Holdsworth, 2022). Previous studies have analyzed calcite cement fill within pull-apart void space. The in situ calcite U–Pb dating yielded an age of 449 ± 15 Ma in the study area (Song et al., 2022). To sum up, we argue that the strike-slip fault formed in the episode III of the middle Caledonian orogeny.

5.1.2. Timing of middle layer structure

The middle layer structure consists of left-stepping syn-depositional normal faults distributed between surfaces T_7^4 and T_6^0, indicating that the faults formed after the Late Ordovician Qiaerbake Formation and before the Late Silurian Keziertage Formation (Fig. 7).

The growth index is near 1 below surface T_7^0, indicating that these en echelon normal faults were not formed before the Sangtamu Formation (Fig. 11). Between surfaces T_7^0 and T_6^3, the growth index is greater than 1, indicating that these normal faults were active during the Kepingtage Formation (Fig. 11). Between surfaces T_6^3 and T_6^0, the growth index of the normal faults is 1.05 in the north and 1.00 in the south (Fig. 11), indicating that the activity gradually weakened and stopped from north to south. We speculate that the formation time of the normal faults was from the Early Silurian to the Late Silurian.

The geological model established by previous structural and geochemical analysis indicates that the fault formed the Silurian (Baqués et al., 2020; Ukar et al., 2020). The in situ calcite U–Pb dating age of calcite cement filled with pull-apart void space is 433 ± 17 Ma (Song et al., 2022). In summary, we believe that the left-stepping normal faults formed in the Late Caledonian orogeny.

5.1.3. Timing of shallow layer structure

The shallow layer structure is characterized by left-stepping normal faults distributed between surfaces T_6^3 and T_5^0, indicating that the faults formed after the Early Silurian Tataaiertage Formation and before the Late Permian Shajingzi Formation (Fig. 7).

It was found that the fault locally displaced the Early-Middle Permian magmatic rocks (Liu et al., 2020; Ukar et al., 2020) (Fig. 12), extended below surface T_5^0, and caused deformation of the overlying strata, suggesting that these faults formed in the Early Permian to Late Permian. We infer that these normal faults formed during the Late Hercynian orogeny.

Based on the above analysis, the SB5 strike-slip fault experienced at least three tectonic movements. The deep, middle, and shallow layer faults formed in the middle Caledonian, late Caledonian, and late Hercynian, respectively (Fig. 13).

5.2. Heterogeneity of fault zone

Fracture frequency, orientation, connectivity, and hydrocarbon production of strike-slip fault-controlled reservoirs in carbonate rocks varies significantly in the Tarim Basin (Y.Y. Li et al., 2018; Wu et al., 2019, 2020). Strike-slip fault zones may be heterogeneous, for example due to lithology, diagenesis, and mechanical properties in the carbonate rock (Gudmundsson et al., 2010; Laubach et al., 2010; Savage & Brodsky, 2011; Faulkner et al., 2011).

5.2.1. Heterogeneity of fault zone width

According to well observations of fracture density, the width of the Ordovician carbonate fault zone can reach 3 km in the Tarim Basin (Ma et al., 2019). The width of the fault zone is of great significance to the scale of the reservoir and oil and gas production (Wu et al., 2019; Wang et al., 2020). We analyzed the heterogeneity of different locations along the fault zone, including single fault segments, extensional overlaps, and contractional overlaps (Fig. 14).

Survey lines 4 and 18 cross the extensional overlaps vertically (Fig. 14a and d). Survey line 4 obtained the width of the fault damage zone of 300 m (Fig. 14a). Here there are three positions where the slope gradient changes. The slope gradient changes at 1550 m and 1850 m represent the boundary of the fault zone. There is a slope gradient change at 1700 m within the fault damage zone. Survey line 18 obtained the width of the fault damage zone of 375 m (Fig. 14d). The fault zone has slope gradient changes at 1950 m and 2025 m. The change of one or two slope gradients in the fault zones indicates the heterogeneous characteristics of the internal damage structure of the extensional overlaps.

Survey lines 7 and 35 cross the fault segments vertically (Fig. 14b and f). The width of the fault damage zone measured by survey line 7 is 175 m and 150 m (Fig. 14b), respectively. The width of the secondary fault damage zone is 150 m. There is no slope gradient change between the main and secondary fault zones. Survey line 35 obtained a width of

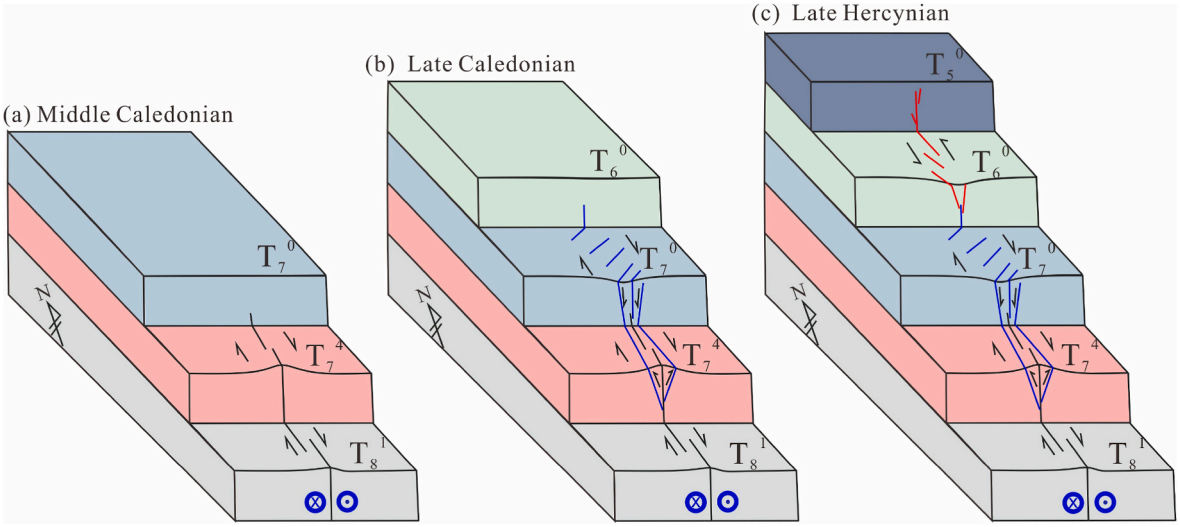

Fig. 13. A schematic model of strike-slip fault evolution within a three-dimensional perspective.

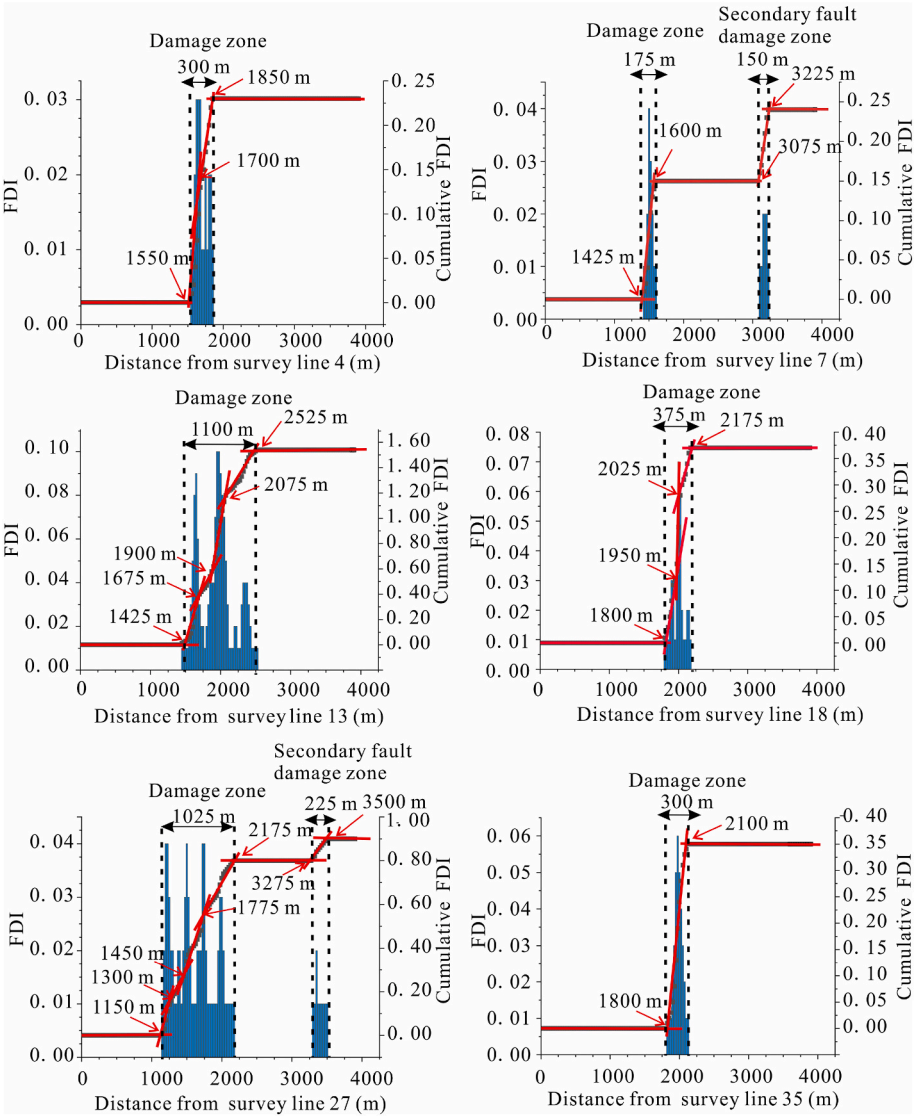

Fig. 14. Cumulative FDI and their slope gradient distribution in different structural styles of the strike-slip fault. (a) Extensional overlap, the width is 300 m. (b) Fault segment, the width is 175 m. (c) Contractional overlap, the width is 1100 m. (d) Extensional overlap, the width is 375 m. (e) Contractional overlap, the width is 1100 m. (f) Fault segment, the width is 300 m.

the isolated fault segment of 300 m (Fig. 14f), and there is also no slope gradient change inside the fault damage zone. No change in the slope gradient within the fault zones indicates that the heterogeneity of the single fault segment is weaker than that of the extensional overlap.

Survey lines 13 and 25 cross the contractional overlaps vertically (Fig. 14c and e). Survey line 13 obtained a fault zone width of 1100 m (Fig. 14c). There are slope changes at 1675 m, 1900 m, and at 2075 m within the fault damage zone. Survey line 27 obtained the width of the fault damage zone of 1025 m (Fig. 14e); the secondary fault damage zone is 225 m. There are three locations with slope gradient changes within the overlapping zone, which are at 1300 m, 1450 m, and 1775 m, respectively. Variation of multiple slope gradients within the overlap zone indicates that the internal heterogeneity of the contractional overlap is stronger than that of the extensional overlap and single fault segment. This finding is consistent with a previous study where patterns were obtained by analogue modeling (Dooley and Schreurs, 2012).

The number of slope gradient change points and the widths indicate that the reservoir heterogeneity of the fault zone varies from high to low in the order contractional overlap, extensional overlap, and single fault segment. This pattern may be related to the process of linkage and interaction between the faults in the evolution process (Fig. 14) (Kim and Sanderson, 2005; Dooley and Schreurs, 2012; Fossen and Rotevatn, 2016; Wu et al., 2019).

5.2.2. Heterogeneity of fracture orientation

In general the distribution of fractures is controlled by rock mechanical properties, structural position, pre-existing structures, and stress field (e.g., Laubach and Ward, 2006; Laubach et al., 2009; Brogi, 2011; Dooley and Schreurs, 2012; Dashti et al., 2018). We analyzed the orientation of the fractures using the image logs, and show that the strike of fractures is mainly in sets that strike NW, NNW, and NNE (Fig. 15). These fractures are characterized by small-angle intersections with the main fault (Fig. 15b). The Riedel shear model can explain this fracture configuration: the NNE-striking fracture direction is an R shear, the NNW-striking fracture set comprises Y shears, and the NW-striking fracture set consitutes P shears. This interpretation is based on analogue modeling results (e.g., Tchalenko, 1970; Naylor et al., 1986; Richard et al., 1995; Dooley and Schreurs, 2012; Peacock et al., 2017). Our study suggests that strike-slip fault-related fractures also have spatial heterogeneity, mainly manifest in fractures that intersect with the main fault strike at a small angle.

5.3. Relationship between fault damage zone width and throw

The scaling of fault attributes (e.g., fault length, displacement, damage zone width, core thickness) has been studied from the core, outcrop, and seismic (Faulkner et al., 2011; Torabi and Berg, 2011; Kolyukhin and Torabi, 2012; Choi et al., 2016; Wu et al., 2020). Many geoscientists argue that a power law is most suitable for describing the distribution of fault attributes (e.g., Kim and Sanderson, 2005; Faulkner et al., 2011; Balsamo et al., 2019). Although there is sufficient evidence to show a positive correlation trend of fault attributes, in most cases, the data plots usually show a discrete distribution of 2-5 orders of magnitude (Knott et al., 1996; Beach et al., 1997; Shipton and Cowie, 2001; Savage & Brodsky, 2011). This scatter may be related to different methods, as well as fault scale, fault type, lithology, deformation background, depth of faulting, diagenesis, and deformation mechanism (e.g., Beach et al., 1997; Kim and Sanderson, 2005; Savage & Brodsky, 2011; Faulkner et al., 2011; Torabi and Berg, 2011; Laubach et al., 2014; Choi et al., 2016; Mayolle et al., 2019).

To ensure the reliability of our results, the top surface of the Middle Ordovician Yijianfang Formation is selected to analyze the width and displacement of the fault zone, which can ensure that the lithology, depth, and deformation background are similar across the study volume. The horizontal displacement of strike-slip faults is difficult to obtain in seismic data, so we analyzed the relationship between widths and throws (Fig. 16). We found that the width has a power law relationship with the throw. There is one order of magnitude scatter in the data (Fig. 16). Compared with previous studies (e.g., Shipton and Cowie, 2001; Faulkner et al., 2011; Torabi and Berg, 2011), the relationship between the width and throw has a smaller order of magnitude change, indicating that there is also a power law relationship between width and throw in these strike-slip faults. The small order of magnitude change may be attributed to the same lithology, depth, and deformation background.

Combining the data of this study with previous data (Ma et al., 2019; Zhao et al., 2021) shows the different scaling trends of fault zone width and throw. Where the throw is less than 100 m, the growth of the width of the fault zone is consistent with the throw. Where the throw is greater than 100 m, the width tends to diminish with the throw, which is consistent with the increase in the slope of the power law relationship between the large fault displacement and width envisaged by Torabi and Berg (2011). This result differs from the 10–100 m slope proposed by Faulkner et al. (2011) and the 2400 m slope proposed by Savage and Brodsky (2011). This diminishing trend may be due to fault interaction

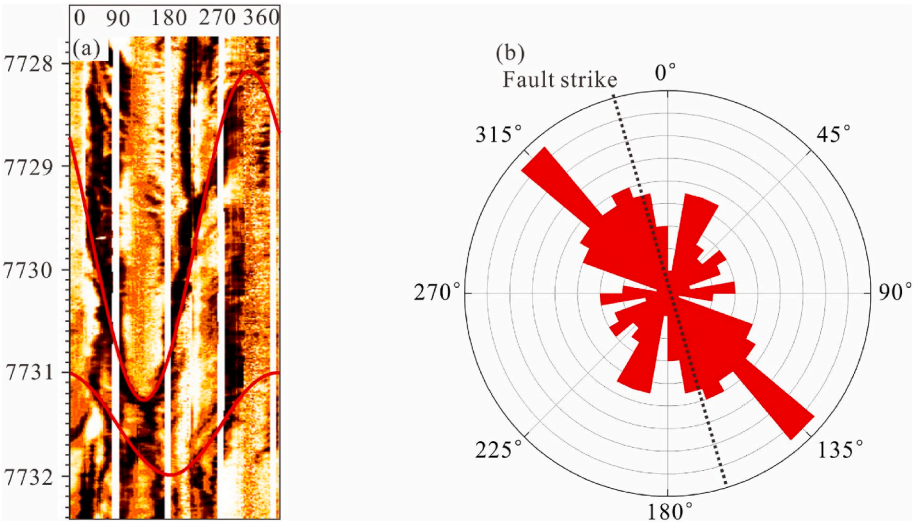

Fig. 15. The strike distribution of fault-related fractures based on imaging logging data. (a) Fracture response characteristics on imaging logging. (b) Strike rose diagram of fault-related fractures. The dotted line indicates the fault strike.

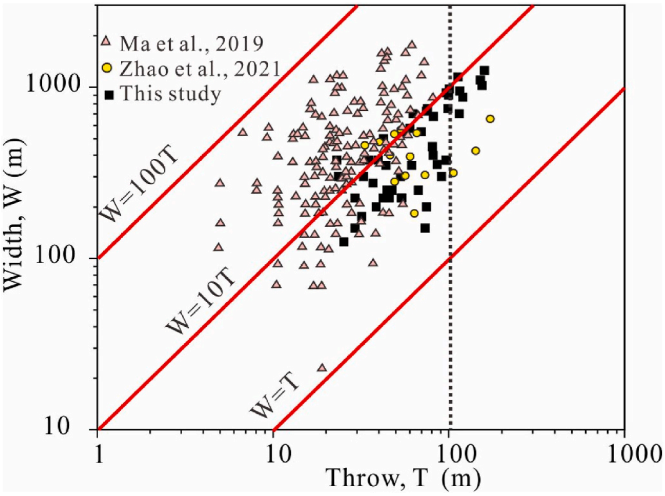

Fig. 16. A compilation of data for fault damage zone width versus throw. When the throw is greater than 100 m, the width tends to slow down with the throw.

and overlapping of active segments (Torabi and Berg, 2011). The ratio becomes smaller for mature faults, possibly due to mechanical interaction between faults or nucleation of secondary faults (Cowie and Scholz, 1992; Willemse et al., 1997; Kim and Sanderson, 2005; Kolyukhin and Torabi, 2012).

6. Conclusions

(1) We propose a fracture development index (FDI) method for analyzing the widths of strike-slip fault zones based on 3D seismic data. We use well data to verify the accuracy of the method to identify the width of the fault zone, and demonstrate that the FDI is reliable for determining the width of the fault zone.

(2) The strike-slip fault we analyzed has different geometric and kinematic characteristics in deep, middle, and shallow structural layers. In map view, at depth the strike-slip fault is characterized by single fault segments, extensional overlaps, and contractional overlaps, at intermediate depths by left-stepping en echelon normal faults, and in shallow layers by right-stepping en echelon normal faults. In cross section, we find composite flower structures and positive flower structures and medium-shallow layer negative flower structures or deep layer negative flower structures and medium-shallow layer negative flower structures. The deep layer strike-slip fault formed in the middle Caledonian orogeny. The middle layer left-stepping normal faults formed in the Late Caledonian orogeny, while the shallow layer right-stepping normal faults formed during the Late Hercynian orogeny.

(3) The strike-slip fault zone is heterogeneous. The heterogeneity of the strike-slip fault zone ranges from strong to weak from contractional overlaps, extensional overlaps, to single fault segments. The strike-slip fault-related fractures are arranged in three sets intersecting with strike-slip faults at small angles that we infer to be R, Y, and P shears.

(4) The fault zone width and throw have a good power law relationship. Where the throw is less than 100 m, the growth of the fault zone width is consistent with the throw. Where the throw is greater than 100 m, the width tends is smaller with the throw.

CRediT author statement

Yingtao Yao: Conceptualization, Methodology, Formal analysis, Investigation, Writing - Original Draft, Writing - Review & Editing. Lianbo Zeng: Writing - Original Draft, Writing - Review & Editing, Supervision, Project administration, Funding acquisition. Zhe Mao and Dongsheng Cao: Visualization, Investigation. Jun Han and Bo Lin: Resources.

Declaration of competing interest

The authors declare that they have no known competing financial interests or personal relationships that could have appeared to influence the work reported in this paper.

Data availability

The authors do not have permission to share data.

Acknowledgements

This paper is supported by the National Natural Science Foundation of China (No. U21B2062). The author highly appreciates the information and support from the Exploration and Development Research Institute of Northwest Oilfield Branch Company, Sinopec. Thank the editor and several anonymous reviewers for their constructive comments, which have significantly contributed to the improvement of this article.

References

Agosta, F., Ruano, P., Rustichelli, A., Tondi, E., Galindo-Zaldívar, J., de Galdeano, C.S., 2012. Inner structure and deformation mechanisms of normal faults in conglomerates and carbonate grainstones (Granada Basin, Betic Cordillera, Spain): inferences on fault permeability. J. Struct. Geol. 45, 4–20.

Aydin, A., 2000. Fractures, faults, and hydrocarbon entrapment, migration and flow. Mar. Petrol. Geol. 17 (7), 797–814.

Balsamo, F., Clemenzi, L., Storti, F., Solum, J., Taberner, C., 2019. Tectonic control on vein attributes and deformation intensity in fault damage zones affecting Natih platform carbonates, Jabal Qusaybah, North Oman. J. Struct. Geol. 122, 38–57.

Baqués, V., Ukar, E., Laubach, S.E., Forstner, S.R., Fall, A., 2020. Fracture, dissolution, and cementation events in ordovician carbonate reservoirs, Tarim Basin, NW China. Geofluids 2020, 1–28.

Beach, A., Lawson Brown, J., Welbon, A.I., McCallum, J.E., Brockbank, P., Knott, S., 1997. Characteristics of fault zones in sandstones from NW England: application to fault transmissibility. Geol. Soc., London, Special Publ. 124, 315–324.

Berg, S.S., Skar, T., 2005. Controls on damage zone asymmetry of a normal fault zone: outcrop analyses of a segment of the Moab fault, SE Utah. J. Struct. Geol. 27 (10), 1803–1822.

Biddle, K.T., Christie-Blick, N., 1985. Strike-slip deformation, basin formation, and sedimentation. SEPM Spec. Publ. 37 (386), 1–34.

Brogi, A., 2011. Variation in fracture patterns in damage zones related to strike-slip faults interfering with pre-existing fractures in sandstone (Calcione area, southern Tuscany, Italy). J. Struct. Geol. 33 (4), 644–661.

Caine, J.S., Evans, J.P., Forster, C.B., 1996. Fault zone architecture and permeability structure. Geology 24 (11), 1025–1028.

Chester, F.M., Evans, J.P., Biegel, R.L., 1993. Internal structure and weakening mechanisms of the San Andreas fault. J. Geophys. Res. Solid Earth 98 (B1), 771–786.

Childs, C., Delogkos, E., Manzocchi, T., Walsh, J.J., 2020. A geological record of changing propagation directions of fault slip events during the growth of a normal fault system. Tectonophysics 774, 228296.

Choi, J.H., Edwards, P., Ko, K., Kim, Y.S., 2016. Definition and classification of fault damage zones: a review and a new methodological approach. Earth Sci. Rev. 152, 70–87.

Cowie, P.A., Scholz, C.H., 1992. Growth of faults by accumulation of seismic slip. J. Geophys. Res. Solid Earth 97, 11085–11095.

Dashti, R., Rahimpour-Bonab, H., Zeinali, M., 2018. Fracture and mechanical stratigraphy in naturally fractured carbonate reservoirs-A case study from Zagros region. Mar. Petrol. Geol. 97, 466–479.

Delle Piane, C., Clennell, M.B., Keller, J.V., Giwelli, A., Luzin, V., 2017. Carbonate hosted fault rocks: a review of structural and microstructural characteristic with implications for seismicity in the upper crust. J. Struct. Geol. 103, 17–36.

Deng, S., Li, H.L., Zhang, Z.P., Zhang, J.B., Yang, X., 2019. Structural characterization of intracratonic strike-slip faults in the central Tarim Basin. AAPG Bull. 103 (1), 109–137.

Dooley, T.P., Schreurs, G., 2012. Analogue modelling of intraplate strike-slip tectonics: a review and new experimental results. Tectonophysics 574, 1–71.

Evans, J.P., 1990. Thickness-displacement relationships for fault zones. J. Struct. Geol. 12 (8), 1061–1065.

Faulkner, D.R., Mitchell, T.M., Jensen, E., Cembrano, J., 2011. Scaling of fault damage zones with displacement and the implications for fault growth processes. J. Geophys. Res. 116 (B5).

Fossen, H., Rotevatn, A., 2016. Fault linkage and relay structures in extensional settings—a review. Earth Sci. Rev. 154, 14–28.
Gudmundsson, A., Simmenes, T.H., Larsen, B., Philipp, S.L., 2010. Effects of internal structure and local stresses on fracture propagation, deflection, and arrest in fault zones. J. Struct. Geol. 32, 1643–1655.
Han, X.Y., Deng, S., Tang, L.J., Cao, Z.C., 2017. Geometry, kinematics and displacement characteristics of strike-slip faults in the northern slope of Tazhong uplift in Tarim Basin: a study based on 3D seismic data. Mar. Petrol. Geol. 88, 410–427.
Harding, T.P., 1985. Seismic characteristics and identification of negative flower structures, positive flower structures, and positive structural inversion. AAPG Bull. 69, 582–600.
Kim, Y.S., Peacock, D., Sanderson, D.J., 2004. Fault damage zones. J. Struct. Geol. 26 (3), 503–517.
Kim, Y.S., Sanderson, D.J., 2005. The relationship between displacement and length of faults: a review. Earth Sci. Rev. 68, 317–334.
Knott, S.D., Beach, A., Brockbank, P.J., Brown, J.L., McCallum, J.E., Welbon, A.I., 1996. Spatial and mechanical controls on normal fault populations. J. Struct. Geol. 18, 359–372.
Klemd, R., John, T., Scherer, E.E., Rondenay, S., Gao, J., 2011. Changes in dip of subducted slabs at depth: petrological and geochronological evidence from HP–UHP rocks (Tianshan, NW-China). Earth Planet Sci. Lett. 310 (1–2), 9–20.
Kolyukhin, D., Torabi, A., 2012. Statistical analysis of the relationships between faults attributes. J. Geophys. Res. Solid Earth 117 (B5).
Laubach, S.E., Eichhubl, P., Hargrove, P., Ellis, M.A., Hooker, J.N., 2014. Fault core and damage zone fracture attributes vary along strike owing to interaction of fracture growth, quartz accumulation, and differing sandstone composition. J. Struct. Geol. 68, 207–226.
Laubach, S.E., Eichhubl, P., Hilgers, C., Lander, R., 2010. Structural diagenesis. J. Struct. Geol. 32, 1866–1872.
Laubach, S.E., Olson, J.E., Gross, M.R., 2009. Mechanical and fracture stratigraphy. AAPG Bull. 93, 1413–1426.
Laubach, S.E., Ward, M.E., 2006. Diagenesis in porosity evolution of opening-mode fractures, Middle Triassic to lower Jurassic La Boca formation, NE Mexico. Tectonophysics 419, 75–97.
Li, D.S., Liang, D.S., Jian, C.Z., Wang, G., Wu, Q.Z., He, D.F., 1996. Hydrocarbon accumulations in the Tarim basin, China. AAPG (Am. Assoc. Pet. Geol.) Bull. 80 (10), 1587–1603.
Li, C.X., Wang, X.F., Li, B.L., He, D.F., 2013. Palaeozoic fault systems of the Tazhong Uplift, Tarim Basin, China. Mar. Petrol. Geol. 39 (1), 48–58.
Li, S.Z., Zhao, S.J., Liu, X., Cao, H.H., Yu, S., Li, X.Y., Somerville, I., Yu, S.Y., Suo, Y.H., 2018. Closure of the proto-tethys ocean and early paleozoic amalgamation of microcontinental blocks in east asia. Earth Sci. Rev. 186, 37–75.
Li, Y.T., Qi, L.X., Zhang, S.N., Yun, L., Cao, Z.C., Han, J., You, D.H., Xiao, H.L., Xiao, C.Y., 2019. Characteristics and development mode of the Middle and Lower Ordovician fault-karst reservoir in Shunbei area, Tarim basin. Acta Pet. Sin. 40 (12), 1470 (in Chinese with English abstract).
Li, Y.Y., Shang, Y.J., Yang, P., 2018. Modeling fracture connectivity in naturally fractured reservoirs: a case study in the Yanchang Formation, Ordos Basin, China. Fuel 211, 789–796.
Liu, G.P., Jiang, B., Guo, R.Q., Gong, X.K., Guo, M., Cui, T., 2020. U–Pb age and Hf isotopic composition of detrital zircons from the modern river of the South Tianshan orogenic belt and their implications for Palaeozoic tectonic and crustal evolution. Geol. J. 55 (10), 7114–7131.
Lyu, H.T., Han, J., Zhang, J.B., Liu, Y.L., Li, Y.T., 2021. Development characteristics and formation mechanism of ultra-deep carbonate fault-dissolution body in Shunbei area, Tarim basin. Petrol. Geol. Exper. 43 (1), 14–22 (in Chinese with English abstract).
Ma, D.B., Wu, G.H., Scarselli, N., Luo, X.S., Han, J.F., Chen, Z.Y., 2019. Seismic damage zone and width–throw scaling along the strike-slip faults in the Ordovician carbonates in the Tarim Basin. Petrol. Sci. 16, 752–762.
Mayolle, S., Soliva, R., Caniven, Y., Wibberley, C., Ballas, G., Milesi, G., Dominguez, S., 2019. Scaling of fault damage zones in carbonate rocks. J. Struct. Geol. 124, 35–50.
Micarelli, L., Moretti, I., Daniel, J., 2003. Structural properties of rift-related normal faults: the case study of the Gulf of Corinth, Greece. J. Geodyn. 36, 275–303.
Mitchell, T.M., Faulkner, D.R., 2009. The nature and origin of off-fault damage surrounding strike-slip fault zones with a wide range of displacements: a field study from the Atacama fault system, northern Chile. J. Struct. Geol. 31, 802–816.
Naylor, M.A., Mandl, G., Supesteijn, C.H.K., 1986. Fault geometries in basement-induced wrench faulting under different initial stress states. J. Struct. Geol. 8, 737–752.
Peacock, D.C.P., Dimmen, V., Rotevatn, A., Sanderson, D.J., 2017. A broader classification of damage zones. J. Struct. Geol. 102, 179–192.
Petit, J.P., Barquins, M., 1988. Can natural faults propagate under mode II conditions? Tectonics 7 (6), 1243–1256.
Qi, L.X., 2021. Structural characteristics and storage control function of the Shun I fault zone in the Shunbei region, Tarim Basin. J. Petrol. Sci. Eng. 203, 108653.
Richard, P.D., Naylor, M.A., Koopman, A., 1995. Experimental models of strike-slip tectonics. Petrol. Geosci. 1, 71–80.
Roberts, N.M.W., Holdsworth, R.E., 2022. Timescales of faulting through calcite geochronology: a review. J. Struct. Geol. 158.
Savage, H.M., Brodsky, E.E., 2011. Collateral damage: evolution with displacement of fracture distribution and secondary fault strands in fault damage zones. J. Geophys. Res. Solid Earth 116 (B3).
Scholz, C.H., Dawers, N.H., Yu, J.Z., Anders, M.H., Cowie, P.A., 1993. Fault growth and fault scaling laws: preliminary results. J. Geophys. Res. Solid Earth 98 (B12), 21951–21961.
Share, P.E., Allam, A.A., Ben-Zion, Y., Lin, F.C., Vernon, F.L., 2019. Structural properties of the San Jacinto fault zone at Blackburn Saddle from seismic data of a dense linear array. Pure Appl. Geophys. 176 (3), 1169–1191.
Shen, Z.Y., Neng, Y., Han, J., Huang, C., Zhu, X.X., Chen, P., Li, Q.Q., 2022. Structural styles and linkage evolution in the middle segment of a strike-slip fault: a case from the Tarim Basin, NW China. J. Struct. Geol. 157, 104558.
Shipton, Z.K., Cowie, P.A., 2001. Damage zone and slip-surface evolution over μm to km scales in high-porosity Navajo sandstone, Utah. J. Struct. Geol. 23, 1825–1844.
Sibson, R.H., 1989. Earthquake faulting as a structural process. J. Struct. Geol. 11 (1–2), 1–14.
Sobel, E.R., Arnaud, N., 1999. A possible middle Paleozoic suture in the Altyn Tagh, NW China. Tectonics 18 (1), 64–74.
Song, G., Li, H.Y., Ye, N., Han, J., Xiao, C.Y., Lu, Z.Y., Li, Y.T., 2022. Types and features of diagenetic fluids in shunbei No. 4 strike-slip fault zone in Shuntuoguole low uplift, Tarim Basin. Petrol. Geol. Exper. 44 (4), 603–612 (in Chinese with English abstract).
Storti, F., Rossetti, F., Läufer, A.L., Salvini, F., 2006. Consistent kinematic architecture in the damage zones of intraplate strike-slip fault systems in North Victoria Land, Antarctica and implications for fault zone evolution. J. Struct. Geol. 28 (1), 50–63.
Sun, Q.Q., Fan, T.L., Gao, Z.Q., G, Wu, J., Zhang, H.H., Qi, Z., Liu, N., Yuan, Y.X., 2021. New insights on the geometry and kinematics of the Shunbei 5 strike-slip fault in the central Tarim Basin, China. J. Struct. Geol. 150, 104400.
Swanson, M.T., 2005. Geometry and kinematics of adhesive wear in brittle strike-slip fault zones. J. Struct. Geol. 27 (5), 871–887.
Sylvester, A.G., 1988. Strike-slip faults. Geol. Soc. Am. Bull. 100 (11), 1666–1703.
Tchalenko, J.S., 1970. Similarities between shear zones of different magnitudes. Geol. Soc. Am. Bull. 81, 1625–1640.
Teng, C.Y., Cai, Z.X., Hao, F., Cao, Z.C., 2020. Structural geometry and evolution of an intracratonic strike-slip fault zone: a case study from the north SB5 fault zone in the Tarim Basin, China. J. Struct. Geol. 140, 104159.
Torabi, A., Berg, S.S., 2011. Scaling of fault attributes: a review. Mar. Petrol. Geol. 28, 1444–1460.
Ukar, E., Baqués, V., Laubach, S.E., Marrett, R., 2020. The nature and origins of decametre-scale porosity in Ordovician carbonate rocks, Halahatang oilfield, Tarim Basin, China. J. Geol. Soc. 177, 1074–1091.
Wang, Z.Y., Gao, Z.Q., Fan, T.L., Shang, Y.X., Qi, L.X., Yun, L., 2020. Structural characterization and hydrocarbon prediction for the SB5M strike-slip fault zone in the Shuntuo Low Uplift, Tarim Basin. Mar. Petrol. Geol. 117, 104418.
Willemse, E.J.M., Peacock, D.C.P., Aydin, A., 1997. Nucleation and growth of strike-slip faults in limestones from Somerset, U.K. J. Struct. Geol. 19, 1461–1477.
Windley, B.F., Allen, M.B., Zhang, C., Zhao, Z.Y., Wang, G.R., 1990. Palaeozoic accretion and Cenozoic redeformation of the Chinese Tien Shan range, central Asia. Geology 18 (2), 128–131.
Wu, C.L., Chen, H.J., Wu, D., Ernst, W.G., 2018. Palaeozoic granitic magmatism and tectonic evolution of the South Altun block, NW China: constraints from zircon U-Pb dating and Lu-Hf isotope geochemistry. J. Asian Earth Sci. 160, 168–199.
Wu, G.H., Gao, L.H., Zhang, Y.T., Ning, C.Z., Xie, E., 2019. Fracture attributes in reservoir-scale carbonate fault damage zones and implications for damage zone width and growth in the deep subsurface. J. Struct. Geol. 118, 181–193.
Wu, G.H., Kim, Y.S., Su, Z., Yang, P.F., Ma, D.B., Zheng, D.M., 2020. Segment interaction and linkage evolution in a conjugate strike-slip fault system from the Tarim Basin, NW China. Mar. Petrol. Geol. 112, 104054.
Yang, S., Wu, G.H., Zhu, Y.F., Zhang, Y.T., Zhao, X.X., Lu, Z.Y., Zhang, B.S., 2022. Key oil accumulation periods of ultra-deep fault-controlled oil reservoir in northern Tarim Basin, NW China. Petrol. Explor. Dev. 49 (2), 285–299.
Yu, Y.X., Tang, L.J., Yang, W.J., Huang, T.Z., Qiu, N.S., Li, W.G., 2014. Salt structures and hydrocarbon accumulations in the Tarim Basin, northwest China. AAPG (Am. Assoc. Pet. Geol.) Bull. 98 (1), 135–159.
Yuan, C., Sun, M., Zhou, M.F., Zhou, H., Xiao, W.J., Li, J.L., 2002. Tectonic evolution of the west Kunlun: geochronologic and geochemical constraints from kudi granitoids. Int. Geol. Rev. 44 (7), 653–669.
Zhang, C.L., Zou, H.B., Li, H.K., Wang, H.Y., 2013. Tectonic framework and evolution of the Tarim block in NW China. Gondwana Res. 23 (4), 1306–1315.
Zhao, Z., Liu, J.T., Ding, W.L., Yang, R.Q., Zhao, G., 2021. Analysis of seismic damage zones: a case study of the ordovician formation in the shunbei 5 fault zone, Tarim Basin, China. J. Mar. Sci. Eng. 9 (6), 630.
Zheng, K., Wu, C.L., Lei, M., Zhang, X., Chen, H.J., Wu, D., Gao, D., 2019. Petrogenesis and tectonic implications of granitoids from western North Altun, Northwest China. Lithos 340, 255–269.